Response to Referee #1

To begin with, we would like to thank the anonymous referee #1 for her/his time and efforts in reviewing our submitted manuscript. We also thank the anonymous referee #1 for her/his constructive comments and suggestions that certainly will improve the manuscript significantly. Finally, we would like to inform the anonymous referee #1 that we will revise the manuscript according to her/his comments and the comments of the anonymous referee #2. Below we respond to the main questions/comments raised by the referee, and outline how we will revise the manuscript. To that end:

- referee's comments are given in blue,

- our responses are outlined in normal format, and

- **any suggested textual changes are given in bold format**.

Responses to general comments (GC) from referee #1 (GC1)

(**GC1.1**) In lieu of implementing a fully- polarized radiative transfer model into the data assimilation scheme, the authors propose to adjust the extinction of "unpolarized" cloud and precipitation scattering properties with an extinction ratio. Such a characterization has sufficient rooting in the body of literature, and it is based on the knowledge that first order scattering effects are the primary mechanism by which clouds and precipitation modify propagating electromagnetic waves. While the overarching approach is well-grounded, there are significant gaps that need to be addressed. The implementation itself is presented more as a fitting exercise with very loose connections to cloud and precipitation physics and the related radiative transfer. The parameterization of the extinction ratio is a bit simplistic, and its application is overgeneralized.

Let us try to summarize our view: This work comprises a first attempt to introduce hydrometeor orientation within a data assimilation (DA) context by improving the physical representation of polarized scattering that was until now completely ignored. Currently, it is too expensive to move towards a fully-polarized radiative transfer in DA, since scattering due to oriented non-spherical hydrometeors increases the complexity of all-sky simulations and substantially increase the computational demands even at non-operational radiative transfer solvers. We introduce an alternative, but physical-based approach that adjusts the extinction as a function of polarization, driven by a special characteristic of the extinction matrix at earth incident angles around 55 ° (zenithal angle of conical scanners): hydrometeor orientation does not change the overall level of extinction. Even if simplified and generalized, this is still a major step forward compared to the situation where the hydrometeor orientation is completely ignored. In the context of fast radiative transfer modelling, particularly in all-sky DA, a special emphasis is given on improving the best fit between model and observations on a global basis and ensuring that improving one aspect does not

lead to a degradation of any other aspect of the DA system (e.g., Geer and Baordo, 2014; Fox, 2020). This context requires simple solutions that could be applied globally. Ideally, the choice of the microphysical representation of the hydrometeors and the selection of the polarization factor would be situation dependent. However, this would increase the intricacy of the forward operator and further complicate any attempts to impartially certify the impact of our choices.

We understand that there are gaps that need to be addressed and hence, we propose to revise the manuscript accordingly, while providing additional clarifications when needed.

Responses to specific comments (SC) from referee #1 (SC1)

(**SC1.1**) Specific comments Lines 92-98: The "microphysical setup" that is used for the RTTOV forward operator is based on manuscript that is in preparation (Geer, 2021), and not available to consider for the review. Salient details are missing, and those details are necessary to properly review this manuscript. Some of this information is basic: What are the size ranges for the different ice habits? But, there are deeper details that need to be considered. The use of a model like Liu's sector snowflake to cover a broad range of ice types makes sense. However, expanding the ice microphysics to multiple ice habits, each with associated high-fidelity scattering properties, offers an opportunity implement a microphysical approach that has a physical basis. While these ice models may be the best numerical matches, the morphologies of the habits selected don't intuitively map to the stated ice classes, with the exception of cloud ice, and there is very little insight into the selection processes.

We feel sorry for any inconvenience caused by the non-availability of Geer (2021), but unforeseen circumstances postponed its submission. Over the last years, several improvements have been implemented in RTTOV-SCATT, the part of RTTOV that accounts for multiple scattering. All these led to RTTOV v13 offering a wider and more physical range of ice hydrometeors (e.g., Eriksson et al., 2018) and particle size distributions (e.g., McFarquhar and Heymsfield, 1997; Petty and Huang, 2011; Heymsfield et al., 2013). Accordingly, the work of Geer (2021) has a dual objective: First, to explore an observation driven methodology for developing parameterizations for clouds and precipitation and, second, to improve the physical representation of ice hydrometeors in RTTOV-SCATT in preparation for the future Ice Cloud Imager (Eriksson et al., 2020) that covers sub-millimetre wavelengths.

In order to fill in any missing parts, we propose to include a separate section, i.e., "Microphysical configuration" and revise Table 1 as follows:

The microphysical setup employed in this study is found in Table 1. This setup was derived by Geer (2021, referred to in that paper as the "intermediate" configuration) using a multi-dimensional parameter search pertinent to ice hydrometeors, i.e., cloud overlap, convective water mixing ratio, PSD, and hydrometeor types for snow, graupel, and cloud ice. The configurations for rain and cloud water were not updated and follow the long-standing configurations for all-sky assimilation at ECMWF (Geer and Baordo, 2014). The search of the "optimal" microphysical setup was treated as a cost minimization problem between observations and simulations on the basis of the Special Sensor Microwave

Table 1. Microphysical setup for all the hydrometeors: PM denotes the particle model, PSD is the particle size distribution, ciw stands for cloud ice water, and clw is the cloud liquid water. $D_{\min}$ and $D_{\max}$ denote the hydrometeor minimum and maximum sizes of the maximum diameter, while a and b comprise the coefficients of the mass-size relation that links the hydrometeor mass (m) to its size (maximum or geometric diameter; D), i.e., $m = aD^b$.

Type	PM	$D_{\min}$ [m]	$D_{\max}$ [m]	a	b	PSD
rain	Mie sphere	1.00e-4	1.00e-2	523.6	3.00	Marshall and Palmer (1948)
snow	Sector snowflake[a] (Eriksson et al., 2018)	1.00e-4	1.02e-2	0.00082	1.44	Field et al. (2007) tropical
graupel	3-Bullet rosette (Liu, 2008)	1.00e-4	1.00e-2	0.32	2.37	Field et al. (2007) tropical
clw	Mie sphere	5.00e-6	1.00e-4	523.6	3.00	Gamma (see, Geer and Baordo, 2014)
ciw	Large column aggregate[b] (Eriksson et al., 2018)	2.42e-5	2.00e-2	0.28	2.44	Heymsfield et al. (2013) stratiform

[a] In Eriksson et al. (2018), the minimum available size of the sector snowflake is 2.00e-5 m, but following Field et al. (2007), a 1.00e-4 m size cutoff has been applied.

[b] The large column aggregate is a mixture of two hydrometeors. Below a size of 3.68e-04 m, it is complemented with the long column single crystals (Eriksson et al., 2018) to provide a complete coverage in size. The name of the mixed hydrometeor follows the one comprising the majority range of size.

Imager/Sounder (SSMIS). The analysis was conducted by means of latitude-longitude bins covering a frequency range of ≈ 19.0–190.0 GHz. The selection of the hydrometeor type was made on the basis of their bulk scattering properties, with the latitude-longitude binning enhancing the spatial differentiation between the three ice hydrometeor types, and the frequency range supporting the latter differentiation owing to the explicit spectral variation of the bulk properties. Each hydrometeor type is parameterized by different a and b coefficients that link the hydrometeor mass (m) to its size (maximum or geometric diameter; D), i.e., mass-size relation ($m = a \cdot D^b$). Accordingly, each hydrometeor leads to a distinct shape of the PSD (e.g., Eriksson et al., 2015) and, consequently, distinct bulk scattering "signature". Although, the morphology of the selected hydrometeors may not be considered as the most physically correct representations, it is only the bulk scattering signature that needs to be correct in the context of DA. The search yielded the following microphysical representation (see Table 1), which was an update on a configuration found by Geer and Baordo (2014). The PSD introduced by Field et al. (2007) (tropical configuration) was retained as a good physical representation for snow and further employed to represent graupel. Snow was previously represented by the sector snowflake by Liu (2008), but it was found that results could be improved with either the ARTS sector snowflake or the ARTS large plate aggregate. Note that the ARTS sector has near identical single scattering properties to Liu's one, but it has less bulk scattering driven by a smaller a coefficient of the mass-size relation. The ARTS large plate aggregate, even though it is characterized by different single scattering properties and mass-size relation, gives (for the chosen PSD) similar bulk scattering properties. This is an illustration why the particle morphology is not yet fully constrained. The choice of the ARTS sector was on the basis that it gave a slightly better fit to observations. For the representation of graupel, similar considerations, particularly to achieve a bulk scattering signature with weak scattering at low frequencies (≈ 50.0 GHz) and strong scattering at high frequencies (≈ 190.0 GHz) led to the selection of the Liu 3-bullet rosette. For cloud ice, the ARTS large column aggregate (LCA) is chosen to replace the physically unrealistic Mie sphere (Geer and Baordo, 2014). Here, the choice of PSD was the main issue, since most of the available PSDs (i.e. McFarquhar and Heymsfield,

1997; Field et al., 2007) were found to generate many large (cm in size) hydrometeors, inducing too much scattering at the highest frequencies considered and leading to rather large discrepancies between observations and simulations. The Heymsfield et al. (2013) PSD was hence chosen as it generates fewer large-size particles. Further, it is constructed on the basis of up-to-date aircraft observations of ice containing clouds (stratiform configuration).

(SC1.2) Table 1: The reference for the sector snowflake should be Liu (2008). Also, following the previous comment, please add the size ranges for each liquid and ice habit.

The reference for the sector snowflake was correct, please see the details given in SC1.1. We will follow the reviewer's comment and include the size ranges of the hydrometeors. Table 1 is the proposed revised table.

(SC1.3) Lines 154-155: The process by which hydrometeors align, and how size relates to alignment needs to be considered in significantly more detail here.

The referee is absolutely right; our description was incomplete. We propose the following revision:

However, ice hydrometeors are characterized by non-spherical shapes and thus non-unit aspect ratios**. This could potentially lead to preferential orientation driven by gravitational and aerodynamical forces (Khvorostyanov and Curry, 2014) or even by electrification processes (lightning activities at deep convective systems, Prigent et al., 2005). Under turbulence-free conditions, small non-spherical hydrometeors (diameters below $\approx 10\,\mu$m) are totally randomly oriented owing to Brownian motion (Klett, 1995); but, if they are large enough, they tend to be horizontally oriented as they fall depending on their shape: this holds true for thick plates with a diameter above $\approx 40\,\mu$m (Klett, 1995), while oblate spheroids and thin plates would adopt horizontal orientation at sizes larger than $\approx 100\,\mu$m (Prigent et al., 2005, and references therein) and $\approx 150\,\mu$m (Noel and Sassen, 2005), respectively. However, turbulent effects can easily disrupt any orientation especially for small hydrometeors or introduce a wobbling motion around the horizontal plane at larger sizes (10–30 μm) (Klett, 1995). In addition, tumbling motions in strong turbulent conditions, e.g., within deep convective cores, induce total random orientation (Spencer et al., 1989).**

(SC1.4) Line 159-161: The salient details of Brath et al. (2020) that are applicable to this manuscript, i.e., a description of the geometry including particle and laboratory reference frames, need to be included. There needs to be enough information to make this paper understandable on its own. As part of this, "tilt" needs to be defined.

We propose to revise this section as follows:

Hydrometeor orientation results in anisotropic scattering with viewing-dependent optical properties, meaning different values of extinction at different polarization components of the incident radiation (dichroism effect, Davis et al., 2005). Accordingly, in vector radiative transfer theory, the attenuation between the incident radiation and the hydrometeor is governed by a 4×4 extinction matrix $\mathbf{K}$, depending on the incident direction and the orientation of the hydrometeor **with respect to a reference system (e.g., Barlakas, 2016). This reference system, or, in other words, the laboratory system is a three-dimensional Cartesian coordinate one that is characterized by a specified position in space and sharing the same origin** as the hydrometeor coordinate system; note that for typical applications, the z axis of the laboratory system would be **aligned with the local vertical direction. Although the selection of the hydrometeor system is arbitrary, it is commonly specified by the shape of the hydrometeor (Mishchenko et al., 1999). In case of an axial symmetry, for example, it is common to align the hydrometeor z axis along the direction of symmetry, with its largest dimension being aligned to the x–y plane (Brath et al., 2020). This acknowledges the tendency for hydrometeors to have horizontal alignment. Now, the orientation of the hydrometeor coordinate system, i.e., hydrometeor orientation, in regard to the laboratory system can be described by the three Euler rotation angles (rotations are applied in order): $\alpha \in [0, 2\pi]$ around the laboratory z axis, $\beta \in [0, \pi]$ around the hydrometeor y axis, and $\gamma \in [0, 2\pi]$ around the hydrometeor z axis (see Fig. 1 in Brath et al., 2020).**

In practice, scattering media consists of an ensemble of hydrometeors with various orientations. Thus, the single **scattering properties should be averaged over all possible orientations to derive the corresponding scattering properties of an ensemble of oriented hydrometeors (Mishchenko and Yurkin, 2017):**

$$\langle f \rangle = \int\limits_{0}^{2\pi} \int\limits_{0}^{\pi} \int\limits_{0}^{2\pi} p(\alpha) \cdot p(\beta) \cdot p(\gamma) \cdot f \, \mathrm{d}\alpha \, \mathrm{d}\beta \, \mathrm{d}\gamma. \tag{1}$$

Where f is a single scattering property (e.g., extinction matrix) at a specific orientation, while $p(\alpha)$, $p(\beta)$, and $p(\gamma)$ describe the probability distributions of the three Euler angles.

In case of TRO, **all possible orientations are equally likely to occur and $p(\alpha)$, $p(\beta)$, and $p(\gamma)$ describe uniform distributions. Consequently,** the extinction matrix has no angular dependency and it is reduced to its first element $K_{\mathrm{TRO}} = K_{11}$, which describes the extinction cross-section **(Mishchenko and Yurkin, 2017; Brath et al., 2020). However, gravitational and/or aerodynamical forces can induce an axial symmetry, with the axis of symmetry specified by the direction of the force (Mishchenko et al., 1999). By aligning the laboratory z axis along the direction of the force, $p(\alpha)$ and $p(\gamma)$ become** uniform distributions resulting in an axial symmetry depending on β, **i.e., tilt angle (Mishchenko et al., 1999). This results in the so-called** azimuth random orientation (ARO)**, describing** a preferred orientation to the horizon based on the tilt angle, with no favored orientation in the azimuth direction (Brath et al., 2020). In this case, **K depends on the incident direction and the tilt angle and it** is reduced to only three independent elements (K_{11}, K_{12}, and K_{34}). K_{12} represents the differences in the extinction between V- and H-polarization (cross section for linear polarization), while K_{34} describes the differences in the extinction between $+45\,^\circ$ and $-45\,^\circ$ polarization (cross section for circular polarization), and is not relevant

here. For a comprehensive description of ARO, the reader is referred to Brath et al. (2020).

(SC1.5) Line 203: One month of data doesn't seem sufficient to represent the full range of brightness temperatures and polarization differences.

155

We acknowledge the referee's concerns with regard to insufficient data. However the literature shows that polarisation signatures are fairly consistent through the seasons and across the globe. Gong and Wu (2017) analyzed six months of GMI data (June, July, and August of 2014 and 2015) at 89.0 and 166.5 GHz and reported that the polarization signatures of ice hydrometeors are fairly consistent across all latitudes, with the only exception being the high latitude belt (70–50 ° S). In a

160 recent paper, Galligani et al. (2021) analyzed one year (2015) of dual polarization observations from GMI and found that the latitudinal and seasonal variations of the polarization patterns of oriented ice hydrometeors are similar and within the standard deviation around the yearly median of the polarization difference. For completeness, we did explore the sample size during the study. However, we based these results on an earlier, slightly different microphysical setup compared to Table 1, so it would be complex to refer to this in the main work. For a polarization ratio $\rho = 1.3125$, we conducted simulations for an additional

165 month, and the resulting statistics were nearly the same for one or two months. To highlight, Table 2 displays the different statistical metrics for the two different months and the corresponding total statistics at 166.5 GHz. Although there are some differences between the time periods, these would not change the conclusions of the paper. Therefore we are confident that the one month sample is fully sufficient.

Following the referee's comment and to avoid any similar conception by any future reader, we propose to include the fol-

170 lowing clarification:

For the passive monitoring experiments, the period of one month was chosen on the basis that polarisation signatures of oriented ice hydrometeors are fairly consistent through the seasons and across the globe (Gong and Wu, 2017; Galligani et al., 2021).

Table 2. Statistical metrics, i.e., mean, skewness, and one dimensional (1D) divergence describing the differences in polarization differences between observations and simulations for a polarization ratio of 1.3125, i.e., $\mathrm{PD^o} - \mathrm{PD^b}$, at 166.5 GHz. Statistics are presented for two time periods, i.e., 13 June to 13 July 2019 and 14 July to 13 August 2019, and their total, i.e., 13 June to 13 August 2019. n stands for the sample size.

Period	n [-]	Mean [K]	Skewness [-]	1D divergence [-]
13 June - 13 July 2019	314379	0.094	1.102	0.726
14 July - 13 August 2019	348353	0.094	1.010	0.617
13 June - 13 August 2019	662732	0.094	1.053	0.741

175

(SC1.6) Line 235: Based solely on Figure 2, why not 1.2? This is certainly within the distribution of the observations, and follows the trend of the observations. especially for combinations of low Tbv and low PD.

180 Following the comment of the reviewer, we suggest the following revision:

The remaining panels in Fig. 2, i.e., b–f, depict the ability of ρ to provide realistic simulations of this behaviour, and a first glance indicates that a ρ value between **1.2 and 1.4 could do a reasonable job, since its within the distributions of the observations.**

185

(SC1.7) Line 259: The higher ratio for 89 GHz compared to 166 GHz doesn't make physical sense, given that polarization differences at 166 GHz are noticeably higher (and the plot in the appendix suggests that the agreement degrades with increased ice scattering).

190 We agree that this may seem unexpected. Given that larger PDs are found at $165.5\,\mathrm{GHz}$ than at $89.0\,\mathrm{GHz}$, it might seem obvious that there should also be a larger polarisation ratio at $165.5\,\mathrm{GHz}$. But this makes the incorrect assumptions that the level of extinction is the same for both frequencies, and that the frequencies are sensitive to the same size range of hydrometeors. But in general, the PD depends on several parameters (size, shape, aspect ratio, PSD) along with the channel's frequency and the level of extinction (Xie and Miao, 2011; Defer et al., 2014). A frequency of $89.0\,\mathrm{GHz}$ samples the PSD at larger sizes

195 compared to $166.5\,\mathrm{GHz}$. Since the axial ratio and thus the amount of preferential orientation increases with size, this could lead to higher PDs at $89.0\,\mathrm{GHz}$ (e.g., Defer et al., 2014). If the extinction was lower at $89.0\,\mathrm{GHz}$, as it would be expected, this would also require higher polarisation ratios to generate the same polarisation difference.

Further, we did mention that the IFS simulates this channel with lower confidence, partly due to its multi-sensitivity aspect that complicates radiative transfer; a frequency of $89\,\mathrm{GHz}$ is quite sensitive to water vapor, water cloud, and rain droplets.

200 Accordingly, even after the carefully surface-screening methods, some of the polarization signal simulated at this frequency could originate from inland water, e.g., large lakes or flooding, that have not been perfectly screened, or even due to shallow clouds over ocean at high latitudes. Similar patterns of potential surface contamination have been recently reported by Galligani et al. (2021). All these, in addition to the known limitations of the IFS and RTTOV-SCATT in representing convective systems (Geer, 2021) could potentially explain the rather large polarization ratio required to obtain reasonable simulations (good fit to

205 the observations) at $89.0\,\mathrm{GHz}$.

To that end, we have lower confidence in the polarization ratio found at $89\,\mathrm{GHz}$. This is the reason why, in the forecast impact and the final configuration of RTTOV-SCATT v13, the polarization ratio found at $166.5\,\mathrm{GHz}$ was adopted.

Nevertheless, following the referee's comment a cautious revision will be conducted in Sections 4.1 and 4.2 to improve clarity.

210

(SC1.8) Figure 4: Looking at this plot, the distribution seems a bit bifurcated (but this *could* be an artifact of insufficient data, referencing previous comment for line 203): one high-slope relationship that contains a large bulk of the data, and another that exhibits significantly more downward curvature with increasing ice scattering. It's also the curve with the lowest Tbv values. The analysis presented in this paper seems to be fitting to the high slope data. It would be instructive to also plot something like 5b here.

As described in Section 4.2, our polarized correction scheme does a reasonable job in reproducing the observed scattering arches, but it is not perfect. RTTOV-SCATT does not simulate the full arch-like relationship because it cannot transfer energy from one polarization to the other (the multiple scattering effect). In addition, Geer (2021) reported that the combination of the IFS and RTTOV-SCATT does not simulate deep enough brightness temperature depressions in tropical convection over land, likely due to insufficient horizontal spreading of the upper glaciated parts of the convective cloud; these scenes, if represented correctly, should have lower PDs according to the hypothesis that turbulence in the deep convective core is responsible for random orientation and hence depolarisation. However, it does reproduce some of the drop in polarization in strongly scattering scenes which is likely due to saturation of the scattering; the differences between τ_H and τ_V become irrelevant. Ideally, the choice of the polarization ratio would be situation dependent. However, this would increase the intricacy of the forward operator and further complicates any attempts to impartially certify the impact of our correction scheme. That said, we do fit the high slope data where most of the points are bundled. However, we will revise the corresponding section to improve clarity.

Following the reviewer's recommendation, we will also include the two dimensional (2D) divergence and revise the text accordingly. The revised figures are Figs. R1 and R2. Panels c display the corresponding 2D divergence, highlighting the areas where RTTOV-SCATT underperforms. In the revised manuscript, we will also update Fig. 3 to include the total 2D divergence as a function of the polarization ratio; see Fig. R3. Note here that a minor bug has been corrected at the same time, whereby points with PDs above 15 K were not fully included in all the plots that display histograms or in the divergence calculations; this bug was not affecting the mean or the skewness derivation. The statistics of the total 2D divergence in Fig. R3 suggest that slightly lower polarization ratios lead to the best agreement between observations and simulations, i.e., 1.45 at 89.0 GHz and 1.35 at 166.5 GHz. However, we stick to the original selection of the "best" polarization ratio due to the skewness. Data assimilation assumes that errors are Gaussian and unbiased; hence we prioritize minimising the measure of skewness, rather than the 2D divergence. In addition, the median and 1D divergence are consistent with the skewness. In the revised manuscript, this additional information will be included.
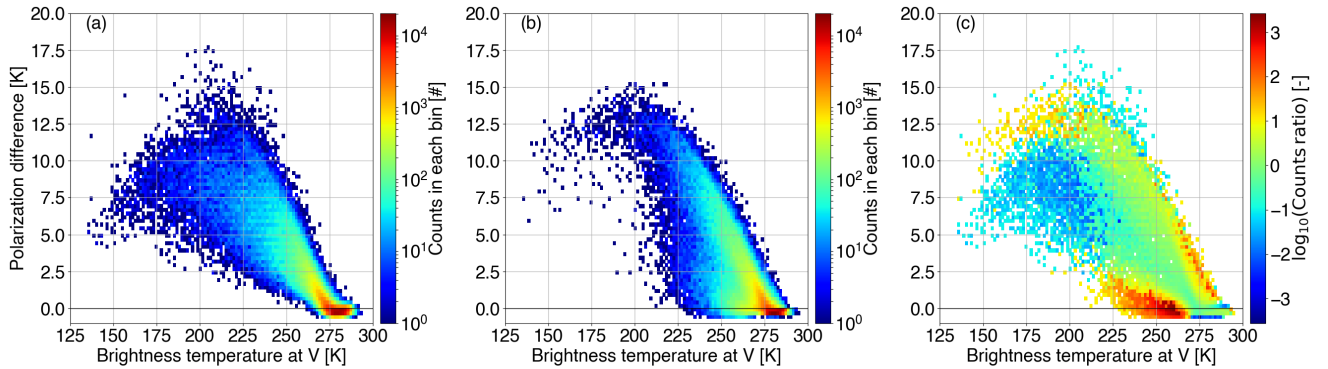
Figure R1. Two dimensional (2D) histograms describing the arch-like relationship between the polarization difference and the brightness temperature at V-polarization at 166.5 GHz as (a) observed ($\mathrm{PD^o} - T_{\mathrm{BV}}^{\mathrm{o}}$) by GMI, (b) simulated ($\mathrm{PD^b} - T_{\mathrm{BV}}^{\mathrm{b}}$) for a polarization ratio of 1.4, and (c) the 2D histogram divergence between $\mathrm{PD^o} - T_{\mathrm{BV}}^{\mathrm{o}}$ and $\mathrm{PD^b} - T_{\mathrm{BV}}^{\mathrm{b}}$. In panel (c), white areas denote the case where both the observed and the simulated 2D bins are empty.
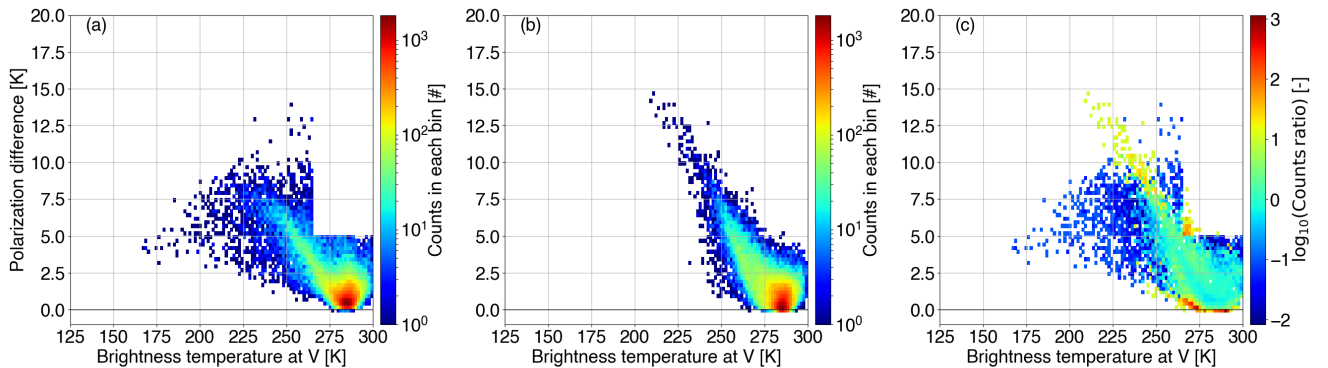
**Figure R2.** As in Fig. R1, but for 89 GHz and a polarization ratio of 1.5.
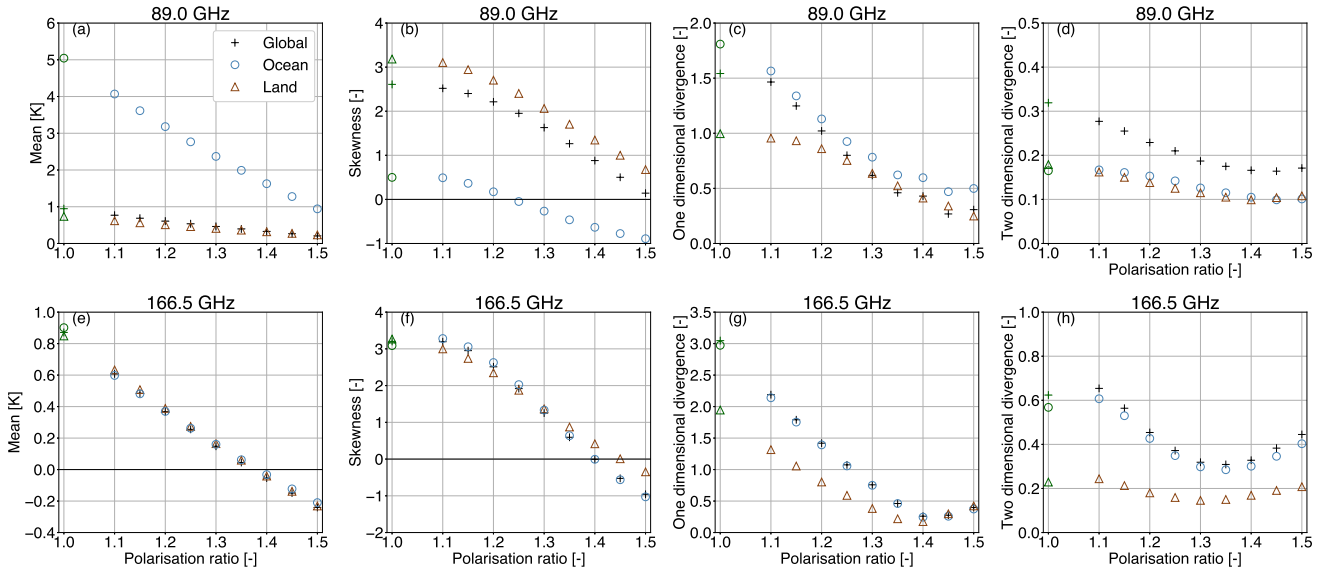
Figure R3. Statistical metrics, i.e., mean, skewness, and one dimensional (1D) divergence describing the differences in polarization differences between observations and simulations, i.e., $\mathrm{PD}^{\mathrm{o}} - \mathrm{PD}^{\mathrm{b}}$ and the two dimensional (2D) divergence between the observed ($\mathrm{PD}^{\mathrm{o}} - T^{\mathrm{o}}_{\mathrm{BV}}$) and simulated ($\mathrm{PD}^{\mathrm{b}} - T^{\mathrm{b}}_{\mathrm{BV}}$) 2D histograms of the arch-like relationship. Results are presented for $89.0\,\mathrm{GHz}$ (top) and $166.5\,\mathrm{GHz}$ (bottom) over land (in brown triangles), ocean (in blue circles), and globally (in black crosses) for a period of one month (13 June to 13 July 2019) as a function of the polarization ratio (ρ). In terms of the control run ($\rho = 1$), the corresponding differences are highlighted in green.

Figure 5: This plot doesn't offer much since this is really a bi-variate distribution, or even better, it should be paired with the mono-variate histograms of Tbv.

Following the reviewer's suggestion, Fig. R4 will represent the updated Fig. 5 (including the minor bug correction), wherein panel (a) highlights the histograms of the brightness temperature at 166.5 GHz as observed (T_B^o; in red) by GMI and simulated (T_B^b) for a polarization ratio of 1.4 (in blue) and 1.0 (in green; control run); solid and dashed lines denote the brightness temperature at vertical and horizontal polarization, respectively, while the shaded area highlights the their difference. Figure R4a also highlights one of the shortcomings described within the manuscript; there is a need to scrutinize the overall level of extinction within the IFS, since it clearly underestimates brightness temperature depressions in tropical convection.

In the revised manuscript, the additional information will be included.
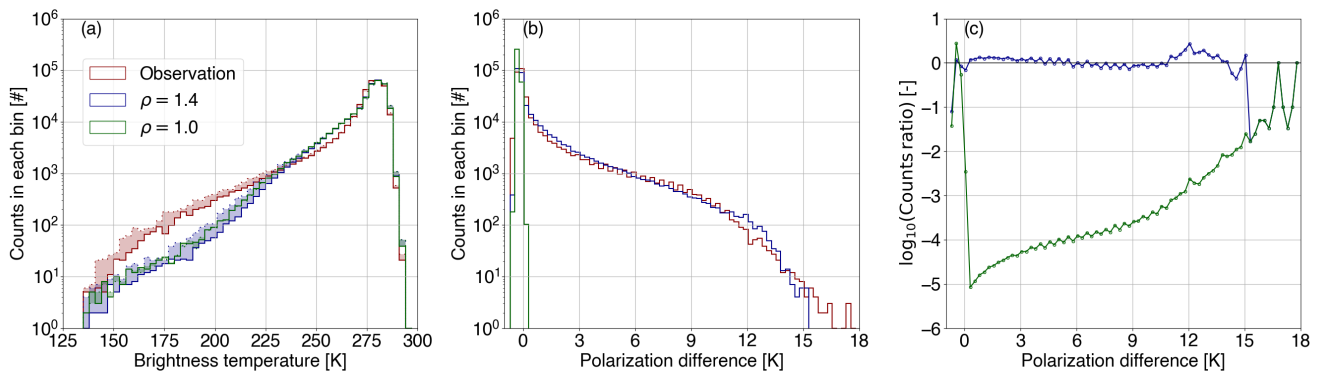
Figure R4. (a) Histograms of the brightness temperature at 166.5 GHz as observed (T_B^o; in red) by GMI and simulated (T_B^b) for a polarization ratio of 1.4 (in blue) and 1.0 (in green; control run); solid and dashed lines denote the brightness temperature at vertical and horizontal polarization, respectively, while the shaded area highlights their difference. (b) Corresponding polarization differences and (c) the divergence between the distributions of PD^o and PD^b as a function of the polarization difference.

(SC1.10) Section 3.4: Overall, this section is a bit confusing, and it doesn't add much in it's current form. Referring to the radiometer bands as numbers (instead of frequency and polarization) definitely make it more opaque. Also, why ATMS? The consideration of polarization is significantly more complicated than the conical scanner, and the polarization ratio has not been characterized over a range of incidence angles which means that the method developed in this paper is not applicable to most of the data.

This comment is not totally understood. In the data assimilation (DA) context, it is important to test whether by improving one aspect, we are not degrading another. This is carried out by validation against independent references, meaning instruments (e.g., ATMS) that are employed in DA, but where a change has not been applied. We do agree that accounting for

polarization is much more complicated for cross-track sounders, but we only apply the correction scheme to all the conical

265   scanners assimilated at ECMWF (three out of the six sensors that are employed in the all-sky assimilation) and where our scheme is applicable. This is already a big step towards a more physical representation of polarized scattering in DA that was previously completely ignored, reducing maximum modelling errors in PD by about 10–15 K, while the remaining errors are now approximately symmetrical.

We do though apologize for any inconvenience caused by referring to some radiometer bands as numbers and hence, in the

270   revised manuscript, this will be resolved. In addition, and we will further clarify the reference to the independent references.

(SC1.11) Line 334: reducing extinction, not scattering.

The text will be revised accordingly.

275

(SC1.12) Lines 340 and 341: again extinction, not scattering.

The text will be revised accordingly.

280   **(SC1.13**) Section 4.1, first paragraph: The description of why the polarization differences approach zero again for deep convection is incomplete. Yes, multiple scattering depolarizes the radiation; however, particle morphologies and orientations within a dynamic environment are also at play: spherical (or less oblate) hail and graupel that may be tumbling in the turbulent environments in which they form, although these processes are not well understood (Jung et al., 2008).

285   The referee is absolutely right; our description was incomplete. We propose the following revision:

The arch-like relationship is generally attributed to **two processes: the saturation of polarisation under conditions of multiple scattering and the composition of the hydrometeors (size, shape, and orientations) within a dynamic environment**. Increasing the number **of large enough ($\approx$ 40–150 μm depending on shape) horizontally oriented non-spherical**

290   **ice hydrometeors (e.g., flat plates, columns, and fluffy snow aggregates) under relatively low turbulence conditions (e.g., stratiform regime or anvil regions of convections)** leads to an increasing scattering, and hence, a stronger polarization signal **(e.g., Spencer et al., 1989; Gong and Wu, 2017; Gong et al., 2020; Brath et al., 2020)**. However, the final polarization state results from only the first few orders of scattering (similar effects are seen at visible frequencies, see, e.g., Barlakas (2016) and references therein). Hence, an increasing multiple-scattering process due to the presence of enough hydrometeors will lead, at

295   first, to a saturation (plateau) of the polarization and, at second, to a further decrease of the PD. Accordingly, the **low** PD values are found at warm T_{BV} ($\approx$ 275 K), corresponding to very thin clouds, while the largest values are linked to intermediate cold T_{BV} and medium thick clouds, particularly in the anvil regions of convection. Within deep convective cores **(at increasingly low T_{BV}), tumbling motions may lead to the formation of less oblate hydrometeors (i.e., hail and graupel, Jung et al.,**

2008), disrupt any hydrometeor orientation inducing either higher tilt angles (see Fig. 1) or even total random orien-
300   **tation, and together with the enhanced multiple-scattering process, lead to low or absent PD ($\approx 0 - 7\,\mathrm{K}$) (e.g., Spencer et al., 1989; Gong and Wu, 2017; Gong et al., 2020)**.

Best regards,

Vasileios Barlakas, Alan J. Geer, and Patrick Eriksson

305 **References**

Barlakas, V.: A new three-dimensional vector radiative transfer model and applications to Saharan dust fields, Ph.D. thesis, https://nbn-resolving.org/urn:nbn:de:bsz:15-qucosa-207467, 2016.

Brath, M., Ekelund, R., Eriksson, P., Lemke, O., and Buehler, S. A.: Microwave and submillimeter wave scattering of oriented ice particles, Atmos. Meas. Tech., 13, 2309–2333, https://doi.org/10.5194/amt-13-2309-2020, https://amt.copernicus.org/articles/13/2309/2020/, 2020.

310 Davis, C. P., Wu, D. L., Emde, C., Jiang, J. H., Cofield, R. E., and Harwood, R. S.: Cirrus induced polarization in 122 GHz aura Microwave Limb Sounder radiances, Geophys. Res. Lett., 32, https://doi.org/10.1029/2005GL022681, https://agupubs.onlinelibrary.wiley.com/doi/abs/10.1029/2005GL022681, 2005.

Defer, E., Galligani, V. S., Prigent, C., and Jiménez, C.: First observations of polarized scattering over ice clouds at close-to-millimeter wavelengths (157 GHz) with MADRAS on board the Megha-Tropiques mission, J. Geophys. Res. Atmos., 119, 12 301–12 316,
315 https://doi.org/10.1002/2014JD022353, https://agupubs.onlinelibrary.wiley.com/doi/abs/10.1002/2014JD022353, 2014.

Eriksson, P., Jamali, M., Mendrok, J., and Buehler, S. A.: On the microwave optical properties of randomly oriented ice hydrometeors, Atmospheric Measurement Techniques, 8, 1913–1933, https://doi.org/10.5194/amt-8-1913-2015, https://amt.copernicus.org/articles/8/1913/2015/, 2015.

Eriksson, P., Ekelund, R., Mendrok, J., Brath, M., Lemke, O., and Buehler, S. A.: A general database of hydrometeor single scattering
320 properties at microwave and sub-millimetre wavelengths, Earth Syst. Sci. Data, 10, 1301–1326, https://doi.org/10.5194/essd-10-1301-2018, https://essd.copernicus.org/articles/10/1301/2018/, 2018.

Eriksson, P., Rydberg, B., Mattioli, V., Thoss, A., Accadia, C., Klein, U., and Buehler, S. A.: Towards an operational Ice Cloud Imager (ICI) retrieval product, Atmos. Meas. Tech., 13, 53–71, https://doi.org/10.5194/amt-13-53-2020, https://amt.copernicus.org/articles/13/53/2020/, 2020.

325 Field, P. R., Heymsfield, A. J., and Bansemer, A.: Snow size distribution parameterization for midlatitude and tropical ice clouds, J. Atmos. Sci., 64, 4346–4365, https://doi.org/10.1175/2007JAS2344.1, https://doi.org/10.1175/2007JAS2344.1, 2007.

Fox, S.: An evaluation of radiative transfer simulations of cloudy scenes from a numerical weather prediction model at sub-millimetre frequencies using airborne observations, Rem. Sens., 12, https://doi.org/10.3390/rs12172758, https://www.mdpi.com/2072-4292/12/17/2758, 2020.

330 Galligani, V. S., Wang, D., Corrales, P. B., and Prigent, C.: A parameterization of the cloud scattering polarization signal derived from GPM observations for microwave fast radiative transfer models, IEEE Trans. Geosci. Remote Sens., pp. 1–10, https://doi.org/10.1109/TGRS.2021.3049921, 2021.

Geer, A. J.: Physical characteristics of frozen hydrometeors inferred with parameter estimation, Atmos. Meas. Tech., p. to be submitted, 2021.

335 Geer, A. J. and Baordo, F.: Improved scattering radiative transfer for frozen hydrometeors at microwave frequencies, Atmos. Meas. Tech., 7, 1839–1860, https://doi.org/10.5194/amt-7-1839-2014, https://www.atmos-meas-tech.net/7/1839/2014/, 2014.

Gong, J. and Wu, D. L.: Microphysical properties of frozen particles inferred from Global Precipitation Measurement (GPM) Microwave Imager (GMI) polarimetric measurements, Atmos. Chem. Phys., 17, 2741–2757, https://doi.org/10.5194/acp-17-2741-2017, https://www.atmos-chem-phys.net/17/2741/2017/, 2017.

340 Gong, J., Zeng, X., Wu, D. L., Munchak, S. J., Li, X., Kneifel, S., Ori, D., Liao, L., and Barahona, D.: Linkage among ice crystal microphysics, mesoscale dynamics, and cloud and precipitation structures revealed by collocated microwave radiometer and multifrequency radar ob-

14

servations, Atmos. Chem. Phys., 20, 12 633–12 653, https://doi.org/10.5194/acp-20-12633-2020, https://acp.copernicus.org/articles/20/12633/2020/, 2020.

Heymsfield, A. J., Schmitt, C., and Bansemer, A.: Ice cloud particle size distributions and pressure-dependent terminal velocities from

345   in situ observations at temperatures from 0° to -86°C, J. Atmos. Sci., 70, 4123–4154, https://doi.org/10.1175/JAS-D-12-0124.1, https://doi.org/10.1175/JAS-D-12-0124.1, 2013.

Jung, Y., Zhang, G., and Xue, M.: Assimilation of simulated polarimetric radar data for a convective storm using the ensemble Kalman filter. Part I: Observation operators for reflectivity and polarimetric variables, Mon. Weather Rev., 136, 2228–2245, https://doi.org/10.1175/2007MWR2083.1, https://journals.ametsoc.org/view/journals/mwre/136/6/2007mwr2083.1.xml, 2008.

350   Khvorostyanov, V. I. and Curry, J. A.: Thermodynamics, kinetics, and microphysics of clouds, Cambridge University Press, https://doi.org/10.1017/CBO9781139060004, 2014.

Klett, J. D.: Orientation model for particles in turbulence, J. Atmos. Sci., 52, 2276–2285, https://doi.org/10.1175/1520-0469(1995)052<2276:OMFPIT>2.0.CO;2, https://journals.ametsoc.org/view/journals/atsc/52/12/1520-0469_1995_052_2276_omfpit_2_0_co_2.xml, 1995.

355   Liu, G.: A database of microwave single-scattering properties for nonspherical ice particles, Bull. Amer. Meteor., 89, 1563–1570, https://doi.org/10.1175/2008BAMS2486.1, https://doi.org/10.1175/2008BAMS2486.1, 2008.

Marshall, J. S. and Palmer, W. M. K.: The distribution of raindrops with size, J. Meteorol., 5, 165–166, https://doi.org/10.1175/1520-0469(1948)005<0165:TDORWS>2.0.CO;2, https://doi.org/10.1175/1520-0469(1948)005<0165:TDORWS>2.0.CO;2, 1948.

McFarquhar, G. M. and Heymsfield, A. J.: Parameterization of tropical cirrus ice crystal size distributions and implications for radiative

360   transfer: results from CEPEX, J. Atmos. Sci., 54, 2187–2200, https://doi.org/10.1175/1520-0469(1997)054<2187:POTCIC>2.0.CO;2, https://doi.org/10.1175/1520-0469(1997)054<2187:POTCIC>2.0.CO;2, 1997.

Mishchenko, M., Hovenier, J., and Travis, L.: Light scattering by nonspherical particles: theory, measurements, and applications, Elsevier Science, 1999.

Mishchenko, M. I. and Yurkin, M. A.: On the concept of random orientation in far-field electromagnetic scattering by nonspherical particles,

365   Opt. Lett., 42, 494–497, https://doi.org/10.1364/OL.42.000494, http://ol.osa.org/abstract.cfm?URI=ol-42-3-494, 2017.

Noel, V. and Sassen, K.: Study of planar ice crystal orientations in ice clouds from scanning polarization lidar observations, J. Appl. Meteorol., 44, 653–664, https://doi.org/10.1175/JAM2223.1, https://journals.ametsoc.org/view/journals/apme/44/5/jam2223.1.xml, 2005.

Petty, G. W. and Huang, W.: The modified gamma size distribution applied to inhomogeneous and nonspherical Particles: Key Relationships and Conversions, J. Atmos. Sci., 68, 1460–1473, https://doi.org/10.1175/2011JAS3645.1, https://journals.ametsoc.org/view/journals/atsc/

370   68/7/2011jas3645.1.xml, 2011.

Prigent, C., Defer, E., Pardo, J. R., Pearl, C., Rossow, W. B., and Pinty, J.-P.: Relations of polarized scattering signatures observed by the TRMM Microwave Instrument with electrical processes in cloud systems, J. Geophys. Res., 32, https://doi.org/10.1029/2004GL022225, https://agupubs.onlinelibrary.wiley.com/doi/abs/10.1029/2004GL022225, 2005.

Spencer, R. W., Goodman, H. M., and Hood, R. E.: Precipitation retrieval over land and ocean with the SSM/I: identifi-

375   cation and characteristics of the scattering signal, J. Atmos. Ocean. Technol., 6, 254–273, https://doi.org/10.1175/1520-0426(1989)006<0254:PROLAO>2.0.CO;2, https://journals.ametsoc.org/view/journals/atot/6/2/1520-0426_1989_006_0254_prolao_2_0_co_2.xml, 1989.

Xie, X. and Miao, J.: Polarization difference due to nonrandomly oriented ice particles at millimeter/submillimeter waveband, J. Quant. Spectrosc. Radiat. Transfer, 112, 1090–1098, https://doi.org/https://doi.org/10.1016/j.jqsrt.2010.11.020, http://www.sciencedirect.com/science/article/pii/S0022407310004437, 2011.